

SPH Study of the Evolution of Water-Water Interfaces in Dam Break Flows

Wei Jian¹, Dongfang Liang², Songdong Shao³, Ridong Chen⁴ and Xingnian Liu⁵

¹ Department of Engineering, University of Cambridge, Cambridge CB2 1PZ, UK. Email: wjian229@gmail.com

² Department of Engineering, University of Cambridge, Cambridge CB2 1PZ, UK. Email: dl359@cam.ac.uk

³ Department of Civil and Structural Engineering, University of Sheffield, Sheffield S1 3JD, UK (State Key Laboratory of Hydro-Science and Engineering, Tsinghua University, Beijing 100084, China). Email: s.shao@sheffield.ac.uk (Author of Correspondence)

⁴ State Key Laboratory of Hydraulics and Mountain River Engineering, Sichuan University, Chengdu 610065, China. Email: chenridong1984@163.com

⁵ State Key Laboratory of Hydraulics and Mountain River Engineering, Sichuan University, Chengdu 610065, China. Email: scucrs@163.com

Abstract

The mixing process of upstream and downstream waters in the dam break flow could generate significant ecological impact on the downstream reaches and influence the environmental damages caused by the dam break flood. This is not easily investigated with the analytical and numerical models based on the grid method due to the large deformation of free surface and the water-water interface. In this paper, a weakly compressible Smoothed Particle Hydrodynamics (WCSPH) solver is used to study the advection and mixing process of the water bodies in two-dimensional dam-break flows over a wet bed. The numerical results of the mixing dynamics immediately after the release of the dam water are found to agree satisfactorily with the published experimental and numerical results. Then further investigations are carried out to study the interface development at the later stage of dam-break flows in a long channel. The analyses concentrate on the evolution of the interface at different ratios between the upstream and downstream water depths. The potential capabilities of the mesh-free SPH modelling approach for predicting the detailed development of the water-water interfaces are fully demonstrated.

Keywords: SPH; dam break; mixing; interface

3 1. Introduction

4
5
6 For free-surface flows, the Smoothed Particle Hydrodynamics (SPH) technique proves to be a
7 promising numerical method in modelling large surface deformations and moving interfaces,
8 even with the presence of water fragmentation and coalescence. Its particle nature provides a
9 straightforward tool for handling complex and moving geometries, since the fluid motion can
10 be easily traced using the Lagrangian description. The SPH method was initially proposed for
11 the astrophysical applications. Lucy (1977) and Gingold and Monaghan (1977) independently
12 modified the Particle-in-Cell (PIC) method to derive a pure particle treatment for the pressure
13 and velocity fields. The particles are linked with each other by a kernel function. Monaghan
14 first extended the SPH application to model incompressible flows with a free surface (1994),
15 in which a weakly compressible assumption was made to model the fluid incompressibility
16 without further computational complication, and an equation of state was used to couple the
17 density and pressure fields. Later studies on the method have extended the application to a
18 variety of hydrodynamic problems. Researches on the surface wave movement, interfacial
19 flow and fluid–structure interaction have demonstrated promising capabilities of the SPH
20 method (e.g. Dalrymple and Rogers, 2006; Violeau and Issa, 2007). In general, it is
21 considered that the SPH method has a great potential for analysing flows involving large
22 deformation, free surface, moving interface, deformable boundary and moving discontinuity.

23
24 Dam-break flows involve the formation of shocks, which arise from the step changes in the
25 initial water level. Under the shallow water assumption, there exist analytical solutions to the
26 problem. However, these may not accurately reflect the actual situations especially in the
27 early stage of the dam break flow, when the large vertical acceleration invalidates the basic
28 foundation of the Shallow Water Equations (SWEs) (Liang, 2010). In recent years, the
29 emphasis of research has shifted to the development of Navier-Stokes (N-S) solvers for the
30 dam-break flows, which have also become a widely used benchmark in the study of the rapid
31 and interfacial flows. Due to its Lagrangian description, the SPH method has been
32 successfully applied to dam-break flows in both two- and three-dimensional configurations.
33 Monaghan (1994) studied a simple dam-break flow to demonstrate the capability of the
34 model. Gómez-Gesteira and Dalrymple (2004) reproduced the impact of the flood wave on a

35 tall structure using a three-dimensional SPH model. The water surface evolutions over dry
36 and wet beds were also analyzed and compared with the experimental data by Crespo (2008)
37 and Crespo et al. (2008). Khayyer and Gotoh (2010) investigated similar problems by using
38 two different mesh-free particle modelling approaches (i.e. MPS/SPH) and evaluated their
39 improved schemes. The major objective of their work is to highlight the potential capabilities
40 of the improved particle numerical schemes in reproducing the detailed features of
41 complicated hydrodynamics. However, their study only focused on the early stage of the dam
42 break flow mixing process and thus the channel length is relatively short. Although very
43 detailed physical mechanisms of dam break flow mixing process have been investigated by
44 Crespo et al. (2008), such as the energy dissipation and vorticity generation, the study is
45 limited by the small spatial and temporal scales of the laboratory test. In addition, Lee et al.
46 (2010) used a three-dimensional WCSPH model to study spillway hydraulics in a practical
47 situation. Furthermore, the two-phase water-sediment mixture interface in a dam break flow
48 was studied by Shakibaeinia and Jin (2011), and water-air interface issue was addressed by
49 Colagrossi and Landrini (2003). More advanced SPH modelling of dam break flows based on
50 the SWEs are attributed to Chang et al. (2011) and Kao and Chang (2012).

51
52 Compared with the pure hydrodynamic studies, the mixing of upstream and downstream
53 waters in dam break flows has been less well understood. The study of dam-break flow
54 mixing process has both theoretical and practical importance in water engineering due to its
55 relevance to the ecological and environmental damages caused by the floods, and the
56 understanding of this process could lead to a better water management and improve the
57 hydro-environmental status of the water system. This paper attempts to numerically model
58 such a mixing process, especially the evolution of the interface between the upstream and
59 downstream waters. As shock waves are always associated with the dam break flows which
60 involve large deformation of free surface and flow interface, the mixing process is a
61 challenge to the traditional analytical and numerical approaches. In this paper, the mesh-free
62 SPH method is applied to the dam-break flow predictions with an emphasis on the associated
63 mixing process. The SPH technique is a mesh-free Lagrangian modelling approach. Its
64 robustness lies in its ability to track the free surfaces and multi-interfaces in an easy and
65 straightforward manner, thus it is well-suited for the study of dam break flow mixing and
66 interface development. The grid modelling techniques solve the hydrodynamic equations on a

67 fixed grid system, thus numerical diffusion and complicated mesh re-configurations are
68 unavoidable when treating the multi-interfaces. In addition, by comparing the numerical
69 solutions with the experimental results, the pros and cons of other alternative numerical
70 approaches for predicting such rapidly varied flows are highlighted.

71

72

73 2. SPH Methodology and Implementation

74

75

76 This section provides a detailed overview of the methodology and implementation of the
77 weakly compressible SPH method, namely the WCSPH method. The SPH formulation is
78 based on the concept of integral interpolations. Using a kernel function to relate the
79 movement of the fluid particles, differential operators in the Navier-Stokes equations can be
80 approximated by summations over the discrete particles. Each particle carries information
81 about the velocity, density, mass, pressure and other flow variables over time (Monaghan,
82 1994).

83

84 In SPH, the approximation of any function $f(\mathbf{r})$ at particle i can be written in terms of the
85 values at neighbouring particles within a compact support zone in the following notation:

$$86 \quad f(\mathbf{r}_i) \approx \sum_j \frac{m_j}{\rho_j} f(\mathbf{r}_j) W_{ij} \quad (1)$$

87 where m_j , ρ_j denote the mass and density of the neighbouring particle j , respectively; \mathbf{r}_j
88 is the spatial position of the particle j and W_{ij} represents the kernel function between particle
89 i and j , $W(\mathbf{r}_i - \mathbf{r}_j, h)$, where h is the smoothing length. As in many hydrodynamic
90 computations, the kernel function used here is the Cubic Spline kernel function. It is a third-
91 order polynomial with a compact support based on a family of spline functions. The
92 smoothing length is often taken to be $h = 1.0 \sim 1.3\Delta r$, where Δr is the initial fluid particle
93 spacing.

94

95 The particle approximation for the spatial derivative of a function can be written with regard
96 to the kernel function as

97
$$\nabla f(\mathbf{r}_i) \approx \sum_j \frac{m_j}{\rho_j} f(\mathbf{r}_j) \nabla_i W_{ij} \quad (2)$$

98 where $\nabla_i W_{ij}$ denotes the gradient of the kernel function with respect to particle i .

99

100 To model incompressible flows, the associated fluid is assumed to be weakly compressible in
 101 order to minimise the computational complication. The continuity equation for a weakly
 102 compressible fluid takes the following form:

103
$$\frac{d\rho}{dt} = -\rho \nabla \cdot \mathbf{v} \quad (3)$$

104 where t is the time and \mathbf{v} is the velocity vector field. The SPH form of the continuity
 105 equation can therefore be derived as:

106
$$\frac{d\rho_i}{dt} = -\rho_i \sum_j \frac{m_j}{\rho_j} (\mathbf{v}_j - \mathbf{v}_i) \cdot \nabla_i W_{ij} \quad (4)$$

107 The momentum equation for a weakly compressible fluid reads:

108
$$\frac{d\mathbf{v}}{dt} = -\frac{1}{\rho} \nabla P + \nu \nabla^2 \mathbf{v} + \mathbf{F} \quad (5)$$

109 where ν is the viscosity coefficient; P is the pressure and \mathbf{F} is the external body force.

110

111 In practice, the pressure gradient is often computed in the following form:

112
$$\nabla P(\mathbf{r}_i) \approx \rho_i \sum_j m_j \left(\frac{P(\mathbf{r}_i)}{\rho_i^2} + \frac{P(\mathbf{r}_j)}{\rho_j^2} \right) \nabla_i W_{ij} \quad (6)$$

113

114 Viscosity is important in improving the stability of the simulation. Instead of discretising the
 115 viscosity term in Equation (5), the artificial viscosity often used in the WCSPH is proposed
 116 by Monaghan (1994) as follows:

117
$$\Pi_{ij} = \begin{cases} \frac{-\alpha \bar{c}_{ij} \mu_{ij} + \beta \mu_{ij}^2}{\rho_{ij}} & \mathbf{v}_{ij} \cdot \mathbf{r}_{ij} < 0 \\ 0 & \mathbf{v}_{ij} \cdot \mathbf{r}_{ij} > 0 \end{cases} \quad (7)$$

118 where $\mu_{ij} = \frac{h \mathbf{v}_{ij} \cdot \mathbf{r}_{ij}}{\mathbf{r}_{ij}^2 + \eta^2}$ and the relevant notations can be found in Monaghan (1994). α is the

119 bulk viscosity and β is the Von Neumann-Richtmyer viscosity. The latter is taken to be zero

120 in present applications. **The artificial viscosity term is introduced to allow for the presence of**

121 shocks and to avoid the particle interpenetration, but the disadvantage is that it may lead to
 122 unphysical decay and diffusion of vorticity in some strong shear flows. Crespo et al. (2008)
 123 adopted a value of coefficient $\alpha = 0.08$ for the dam break mixing flows and it was later
 124 found by Khayyer and Gotoh (2010) that the simulations could lead to excessive vorticity
 125 dissipation. They obtained more stable results when decreasing the coefficient from 0.08 to
 126 0.02. By balancing the viscous decay and the integrity of free surface profiles, a value of 0.02
 127 was used for all the applications presented in this paper.

128

129 In order to close the equation systems, an equation of state has been adopted to relate the
 130 pressure to the density. For water it takes the following form

$$131 \quad P = B \left(\left(\frac{\rho}{\rho_0} \right)^\gamma - 1 \right) \quad (8)$$

132 where ρ_0 is the reference density that is usually set to 1000.0 kg/m³ for water; and γ is a
 133 constant that is normally taken to be 7. The parameter B sets a maximum limit for the density
 134 variation allowed in the flow. It is calculated based on $c_0^2 \rho_0 / \gamma$, where c_0 is the speed of
 135 sound at the reference density.

136

137 The particle positions are updated using the velocity calculated from the momentum equation.
 138 In practical computations, the following XSPH variant is used to increase the numerical
 139 stability and accuracy

$$140 \quad \frac{d\mathbf{r}_i}{dt} = \mathbf{v}_i - \varepsilon \sum_j \frac{m_j}{\rho_j} \mathbf{v}_{ij} W_{ij} \quad (9)$$

141 where ε is a constant in the range between 0.0 and 1.0 depending on the application. **In this**
 142 **paper, ε is taken as 0.5 following Crespo et al. (2008). In most dam break flow simulations,**
 143 **ε has been taken to be around 0.5 to achieve the best performances (Monaghan, 1994).**
 144 **However, we should realize that the increase of this value may lead to more numerical**
 145 **smoothing effect, so attentions should be paid to calibrate the optimum value for small**
 146 **amplitude waves.**

147

148 The time integration procedures of the continuity and momentum equations follow the
 149 modified predictor-corrector Euler scheme (Monaghan, 1994). Owing to the large sound
 150 speed required for the weakly compressible assumption, very small time step is needed in the
 151 WCSPH model to satisfy the CFL condition. In this paper, all of the WCSPH computations
 152 are based on an in-house code developed in Liang (2010) and Liang et al. (2010).

153
 154 The initial setting of the particle positions plays an important role in the accuracy and
 155 computational efficiency of the SPH method. In WCSPH, a common practise is to first
 156 conduct a numerical simulation under the hydrostatic condition until the movement of
 157 particles becomes very small, and then the actual dynamic simulation starts. On the solid
 158 boundaries, the non-penetration condition must be satisfied. In the present work, the
 159 Lennards-Jones repulsive force method is used in the WCSPH model for its simplicity and
 160 effectiveness. On the free surface, both kinematic and dynamic boundary conditions can be
 161 automatically met by the Lagrangian nature of the SPH method.

162
 163 It has been noticed that the summation interpolant fails to reproduce a constant function in
 164 some actual simulations, which often leads to unphysical variation of the local density field
 165 especially near the boundaries. In the WCSPH model used in this work, the Shephard
 166 filtering is performed every 40 time steps to reinitialize the density field. Hence, the
 167 numerical stability is maintained. One of the major instabilities experienced by the SPH
 168 model is the particle clumping in certain simulations. Monaghan (2000) introduced an
 169 additional term, f_{ij} , into the momentum equation to exert a repulsive force between the fluid
 170 particles with small separations. This force is dependent on the kernel function and the
 171 pressure field, which takes the form of

$$172 \quad f_{ij} = 0.01 \left(\frac{P_i}{\rho_i^2} + \frac{P_j}{\rho_j^2} \right) \left(\frac{W_{ij}}{W(\Delta r)} \right)^n \quad (10)$$

173 where $W(\Delta r)$ is the kernel function value based on the initial particle spacing; and n is a
 174 constant normally set at 4. Finally, the momentum equation (5) in SPH form becomes

$$175 \quad \frac{d\mathbf{v}_i}{dt} = -\sum_j m_j \left(\frac{P_i}{\rho_i^2} + \frac{P_j}{\rho_j^2} + \Pi_{ij} + f_{ij} \right) \nabla_i W_{ij} + \mathbf{g} \quad (11)$$

176 where the external force term includes the gravitational acceleration \mathbf{g} only.

177 **3. Model Validations: Dam-break Flow Propagation**

178

179

180 In this section, the propagation of a dam-break flow is simulated and validated against the
181 experimental work detailed in Stansby et al. (1998), the analytical solutions to the Shallow
182 Water Equations and the numerical solutions to the Navier-Stokes equations using the
183 Volume of Fluid (VOF) method (Jian, 2013), **in which FLUENT13.0 is used and thus the**
184 **numerical scheme is based on the Finite Volume method.** The test case considers the
185 instantaneous collapse of a dam in a wide, horizontal and frictionless channel of 200 m long.
186 Water is initially static and separated by a gate located at $x = 100$ m. The initial conditions are
187 defined as:

$$188 \quad u(x,0) = 0, \quad h(x,0) = \begin{cases} h_1 & \text{if } x > 100 \text{ m} \\ h_0 & \text{if } x \leq 100 \text{ m} \end{cases} \quad (12)$$

189 where h_0 is the initial water depth upstream of the dam; and h_1 is the initial water depth in
190 the downstream channel. In this study, the upstream water depth h_0 is kept constant at 10.0 m,
191 while three different values have been considered for h_1 : 0.0 m for a dry bed, 1.0 m for a
192 shallow wet bed, and 4.5 m for a deep wet bed, respectively.

193

194 The parameters used in the WCSPH model are: initial particle spacing $\Delta r = 0.1$ m and time
195 step $\Delta t = 0.0002$ s. In the grid-based VOF model, the main computational parameters are:
196 grid size of 0.1×0.1 m² and time step $\Delta t = 0.005$ s. Hence, the spatial resolutions of the
197 mesh-free and grid-based models are comparable.

198

199 **3.1 Results and discussions**

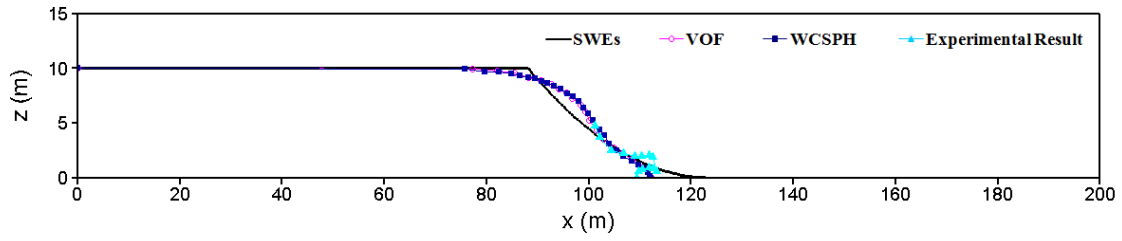
200

201 Figures 1 to 3 illustrate the comparisons among the numerical results of the WCSPH model,
202 the experimental data of Stansby et al. (2008), analytical solutions to the SWEs (Jian, 2013)
203 and numerical solutions to the Navier-Stokes equations using the VOF method (Jian, 2013),
204 with the initial downstream water depths being $h_1 = 0.0$ m, 1.0 m and 4.5 m, respectively.

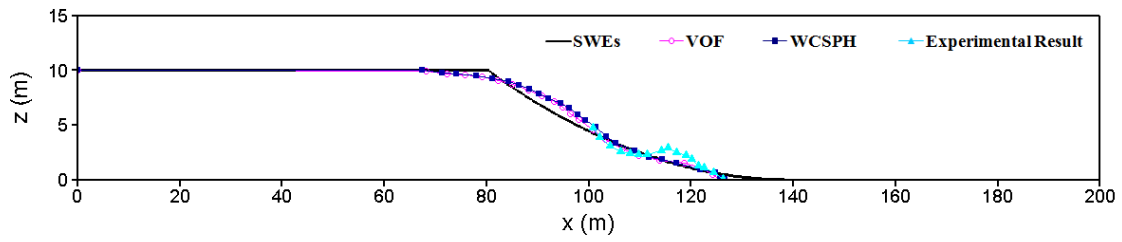
205

206

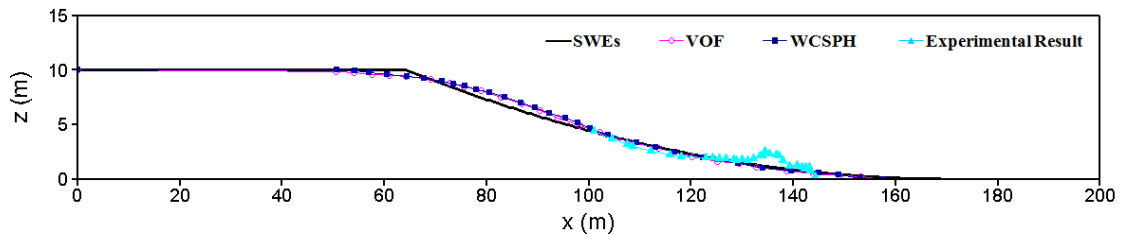
207



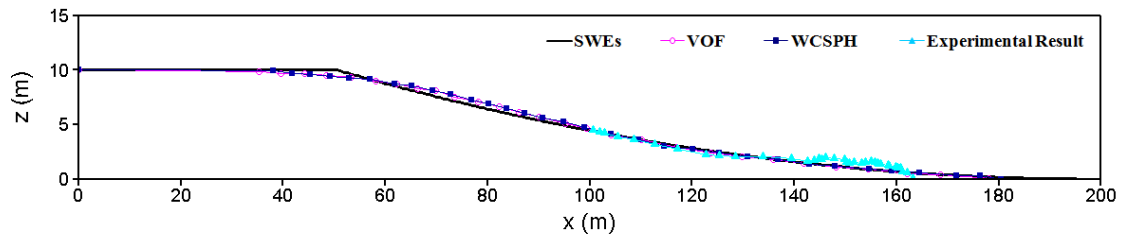
208
209



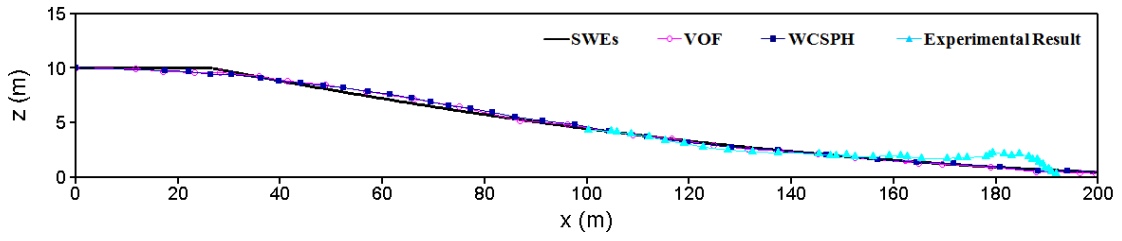
210
211



212
213



214
215



216
217
218

219 **Figure 1** Free surface profiles in the dam-break flow over dry bed $h_1 = 0.0$ m, at $t = 1.20$ s,

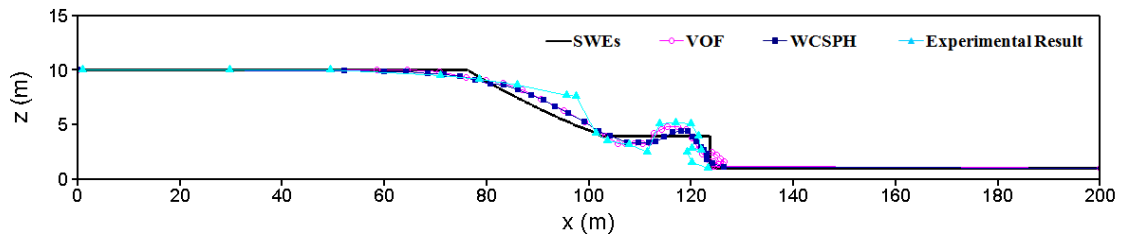
220

2.00 s, 3.60 s, 5.00 s and 7.40 s, respectively

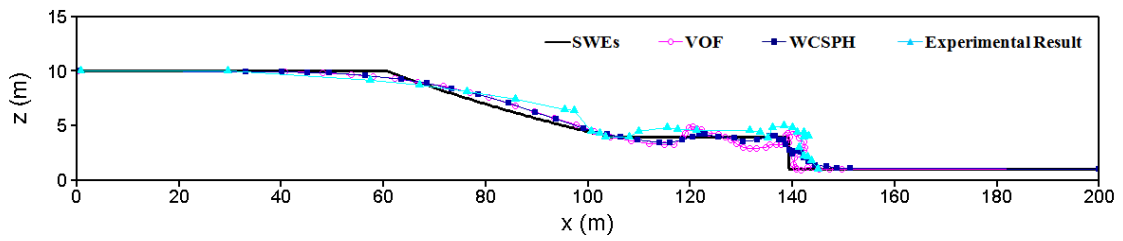
221

222

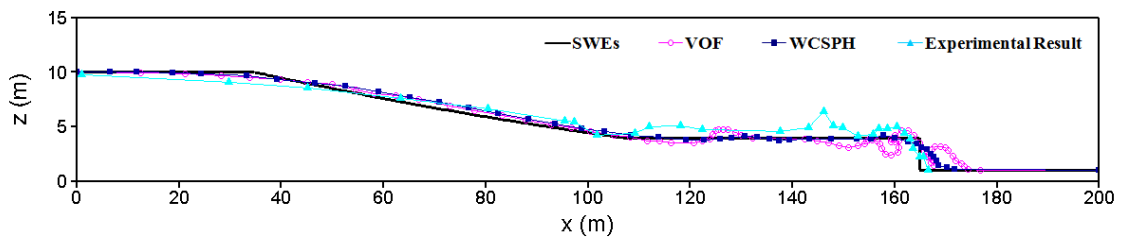
223



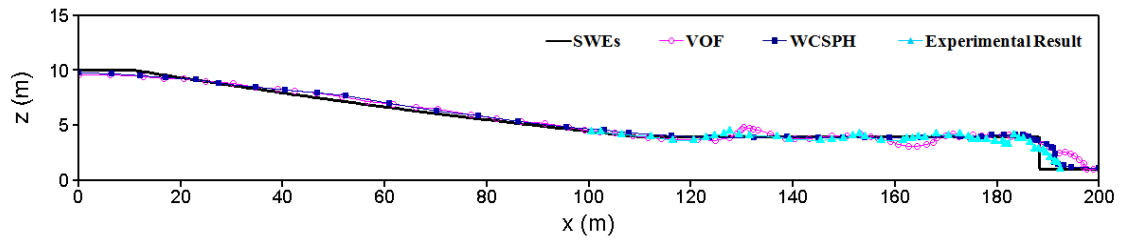
224
225



226
227



228
229



230
231

232

233

Figure 2 Free surface profiles in the dam-break flow over shallow wet bed $h_1 = 1.0$ m, at $t =$

234

2.40 s, 4.00 s, 6.60 s and 9.00 s, respectively

235

236

237

238

239

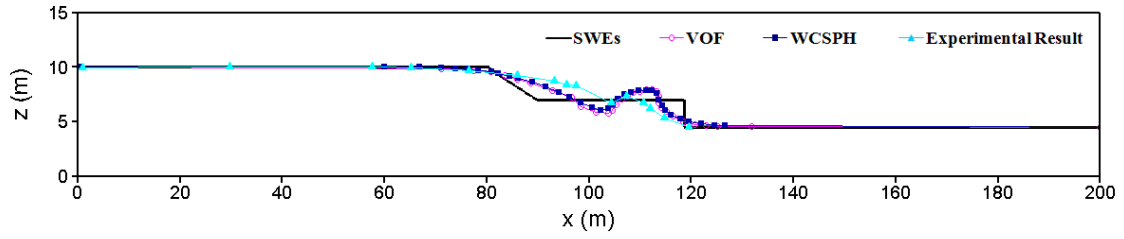
240

241

242

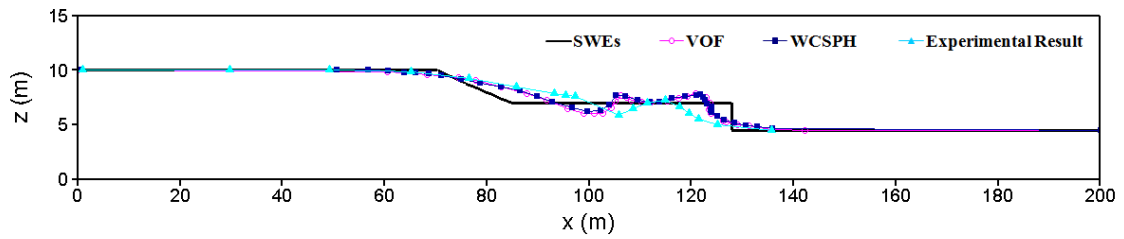
243

244



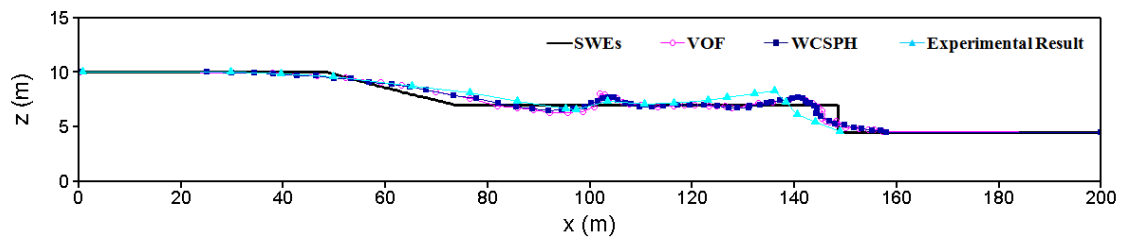
245

246



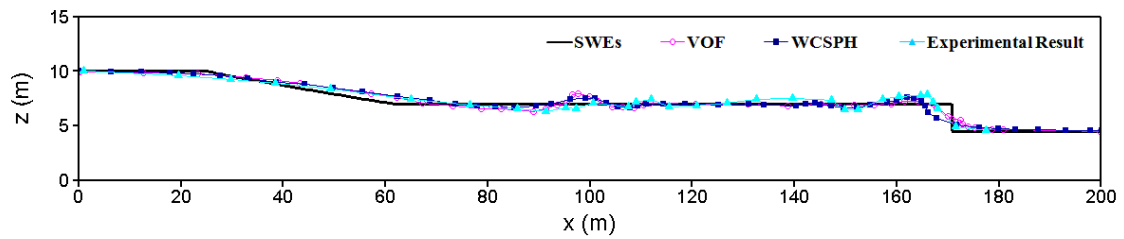
247

248



249

250



251

252

253 **Figure 3** Free surface profiles in the dam-break flow over deep wet bed $h_1 = 4.5$ m, at $t =$

254

2.00 s, 3.00 s, 5.20 s and 7.60 s, respectively

255

256

257

258

259

260 It is seen from Figures 1 to 3 that the flow caused by the collapsed dam behaves very
261 differently depending on the downstream depths. For a dry bed, the forward momentum
262 dominates the fluid movement and the flood front is established very quickly. Figure 1 shows
263 that, by $t = 1.20$ s, the wave front has already settled into a stable form and its propagation
264 for the rest of simulation is free of any breaking. If there is initially a layer of water in the
265 downstream channel, the upstream water can build up into the front with a significant height.
266 A mushroom-like waveform emerges in both Figures 2 and 3 immediately after the dam
267 collapses. The downstream condition generally determines the shape of the wave front that
268 propagates downstream. If the initial downstream water depth is shallow, the accumulated
269 water front soon breaks onto the static water in the channel, driven by the large pressure
270 gradient as shown in the surface profile at $t = 6.60$ s in Figure 2. The broken wave front
271 continues to travel downstream, accompanied by some small-scale breakings at the interface
272 between the reservoir water and the channel water. The overall waveform under the shallow
273 water layer condition is characterised by the water front travelling downstream. This is,
274 however, not the case in the deep downstream water condition as shown in Figure 3, in which
275 the mushroom-like water front seen at $t = 2.00$ s gradually evolves into two distinct wave
276 forms travelling in the opposite direction. The experimental data suggests that the
277 downstream-propagating water front is slightly more prominent, whereas the numerical
278 results indicate a more balanced strength between the two wave fronts.

279
280 All of the three scenarios observe a good agreement between the WCSPH and VOF
281 computations against the experimental data. Both models are based on the Navier-Stokes
282 equations and are able to predict the propagation of the dam-break flow with good accuracy.
283 However, slight discrepancies exist in the propagation speed between the experimental
284 observations and numerical predictions. Due to the assumption of frictionless solid
285 boundaries, the propagation of the wave front is over-predicted under the dry bed condition.
286 In addition, the numerical predictions tend to estimate a more rapid wave front development
287 under the deep downstream water layer setting. For all three cases, the solutions to the SWEs
288 deviate significantly from the experimental observations immediately after the dam collapse.
289 This is because the SWEs are only able to provide approximate predictions of the free surface
290 when there is insignificant variation in the vertical direction (Liang, 2010). Therefore, some
291 of the key features observed in the experimental results are lost in the SWEs predictions.

292 Despite this, the propagation speed of the wave front agrees well with the experimental data,
 293 except that a slight over-estimation is found for the case of the deep ambient layer. Once the
 294 flow has settled into an established form at the later stage, the accuracy of the SWEs
 295 prediction improves significantly as the flow characteristics satisfy the underlying long-wave
 296 assumptions adopted in deriving the SWEs. Similar observations have also been reported in
 297 Pu et al. (2013).

298

299 One distinct advantage of the WCSPH model is its superior computational efficiency over the
 300 VOF model for the three cases considered here. Table 1 lists the CPU time required for
 301 simulating the cases using the WCSPH and VOF models. Since the VOF method needs to
 302 simulate the flow of both the water and air phases, it requires a significantly longer
 303 computational time.

304

305 **Table 1 CPU time required for the dam-break flow simulations**

306

Test case	Physical time (s)	CPU time (hr)	
		WCSPH	VOF
Dry bed ($h_0 = 10.0$ m and $h_1 = 0.0$ m)	7.40	3.10	11.30
Shallow wet bed ($h_0 = 10.0$ m and $h_1 = 1.0$ m)	9.00	4.08	14.15
Deep wet bed ($h_0 = 10.0$ m and $h_1 = 4.5$ m)	7.60	4.96	17.12

307

308

309

310 **4. Model Application: Mixing Process in Near-field Dam-break Flows**

311

312

313 From the model validations in the previous section, we understand that, in the case of a wet
 314 downstream bed, the collapsed water undergoes a dynamic interaction with the water body
 315 downstream, which incurs significant mechanical energy dissipation. This section pays
 316 particular attention to the mixing process involved in dam-break flows. Ignoring the

317 molecular diffusion, the mixing of the water bodies can be considered as the non-uniform
318 advection of the water associated with the violent wave movements. Here, we apply the
319 WCSPH model to focus on the mixing process involved in the early stage of dam-break flows.
320 The numerical results are compared with the published experimental results. We need to
321 mention that no advanced turbulence closures are included in the WCSPH model, except the
322 artificial viscosity mentioned before. **The term of near-field indicates the mixing process**
323 **situation immediately after the dam break when the interface between the reservoir water and**
324 **tail water is very complicated.**

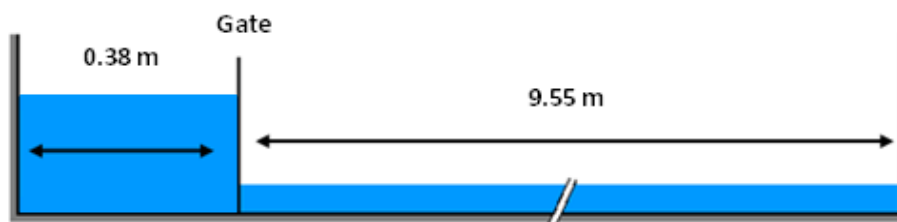
325

326 **4.1 Model setup and computational parameters**

327

328 The validation case examines the interaction between two water bodies in a dam-break flow
329 problem immediately after the release of the dammed water. The numerical study is based on
330 the experiment in Janosi et al. (2004). Figure 4 shows the experimental setup of a two-
331 dimensional flume with two compartments separated by a gate at $x = 0.38$ m. A volume of
332 water with a height of 0.15 m (h_0) is initially locked up in the upstream compartment. The
333 gate is gradually lifted up at a removal rate of approximately 1.5 m/s after the experiment
334 starts, allowing the initially locked water to seep through the opening. Several different
335 downstream depths are considered: shallow ambient layer with depth $h_1 = 0.015$ m and deep
336 ambient layer with $h_1 = 0.030$ m, 0.058 m and 0.070 m, respectively.

337



338

339

340 **Figure 4 Experimental setup of the dam-break flow in Janosi et al. (2004)**

341

342 To increase computational efficiency, a shorter computational domain was adopted in the
343 model. Since the physical time of interest is 0.6 seconds in total, the downstream channel

344 length can be reduced to 2.5 m without affecting the results. In the SPH computations, the
345 initial particle spacing is $\Delta r = 0.001$ m in the shallow depth condition and 0.002 m in the
346 deep depth condition. The corresponding time steps are $\Delta t = 1.0 \times 10^{-5}$ s and 2.0×10^{-5} s,
347 respectively. The gate is modelled by a set of repulsive particles, with their positions and
348 velocities externally specified to resemble the removal procedure. The two water bodies are
349 tracked by assigning different flags to the upstream and downstream water particles at the
350 beginning of the simulation so that the mixing interface can be identified as the separation of
351 the particles carrying different flags.

352

353 **4.2 Results and discussions for the shallow ambient layer**

354

355 The WCSPH results and the experimental observations (Janosi et al., 2004) are compared in
356 Figure 5 for the case of the shallow ambient layer depth $h_1 = 0.015$ m. It is evident that the
357 numerical model is able to reproduce the wave propagation after the gradual removal of the
358 gate. The main features observed in the experimental snapshots, such as the formation of a
359 mushroom-like water jet and the subsequent wave breakings, are resembled in the numerical
360 predictions with reasonable accuracy. There are some discrepancies in the mixing profiles
361 between the experimental and numerical results. The mixing interface observed during the
362 experiment remains relatively vertical throughout the time with only a slight sloping towards
363 the downstream direction at $t = 0.392$ s. In addition, the profiles at $t = 0.327$ s and 0.392 s
364 suggest that the plunging wave front is mostly composed of channel water. The numerically
365 predicted interfaces exhibit varying degrees of inclination towards the downstream in their
366 mixing profiles. However, the overall agreement is still satisfactory.

367

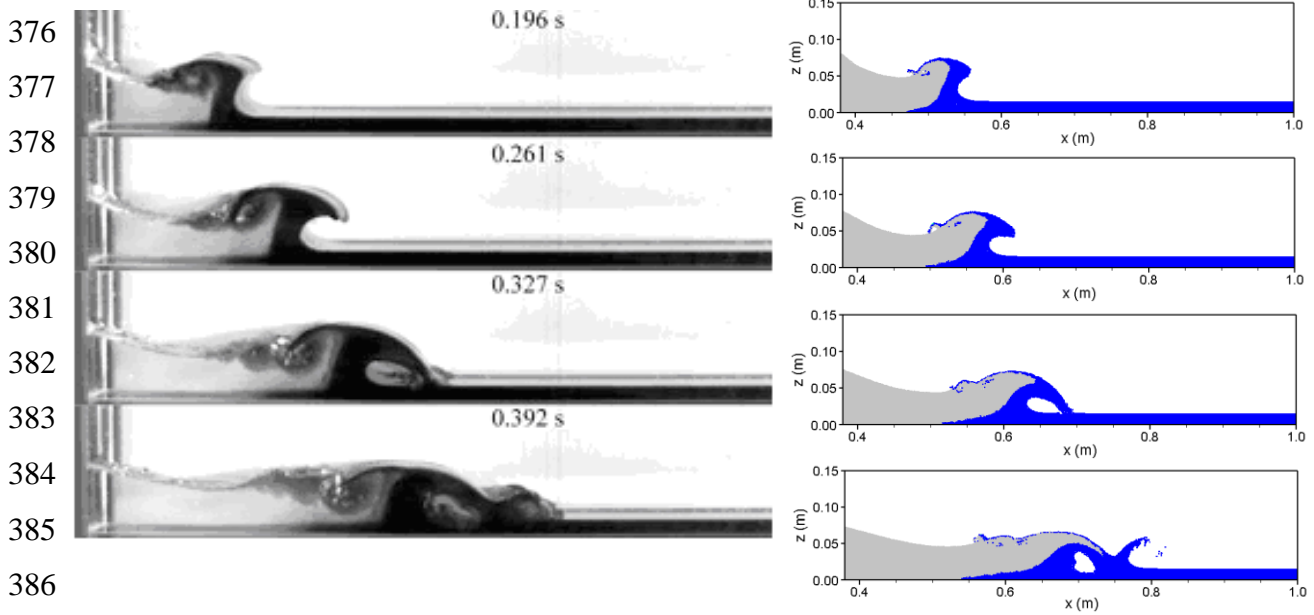
368 Another key feature observed in the mixing patterns is the presence of a thin layer of
369 downstream water at the surface upstream of the plunging water front. That water is brought
370 to the surface by an up-thrust movement during the initial collision of the two water bodies.
371 The WCSPH model is able to capture the presence and development of this thin water layer.

372

373

374

375



388 **Figure 5 Experimental (left, Janosi et al., 2004) and numerical (right) mixing patterns at**
 389 **$t = 0.196$ s, 0.261 s, 0.327 s and 0.392 s for shallow flow depth $h_1 = 0.015$ m**

391 4.3 Results and discussions for the deep ambient layers

392 Three large downstream flow depths have been analysed, i.e. $h_1 = 0.030$ m, 0.058 m and
 393 0.070 m. Figure 6 presents the experimental snapshots and numerical predictions of the
 394 mixing patterns at $t = 0.30$ s. It is shown that with the increased downstream water depth, the
 395 collision between the two water bodies and the subsequent breaking exhibit quite different
 396 characteristics from those shown in the shallow ambient layer condition.
 397

398
 399 With $h_1 = 0.030$ m, the wave front shows an established mushroom-like shape at $t = 0.30$ s.
 400 The formation of the waveform is slower when compared with the case in Figure 5 for the
 401 shallow layer. Generally speaking, the SPH simulations show a satisfactory agreement with
 402 the experimental results at $t = 0.30$ s. The discrepancy lies in the amount of downstream
 403 water at the surface. The experimental snapshot suggests that the downstream water makes up
 404 approximately half of the plunging wave column, whereas the numerical prediction only
 405 shows a relatively thin layer at the free surface which is similar to the case of the shallow
 406 ambient layer. Figure 6 also shows that the waveforms take longer time to fully develop with

407 increasing downstream water depth. The experimental snapshots for $h_1 = 0.058$ m and 0.070
 408 m suggest that the wave fronts are still gaining their height at this instant. In addition, the
 409 corresponding mixing interfaces take different shapes to the ones studied previously. It
 410 closely resembles a straight line for $h_1 = 0.058$ m, while inclines slightly towards the
 411 upstream direction with $h_1 = 0.070$ m. Again, the WCSPH model demonstrates a good
 412 estimation of the mixing feature at the free surface. Consistent with the case for $h_1 = 0.030$ m,
 413 the model underestimates the amount of mixing upstream of the wave front.

414

415

416

417

418

419

420

421

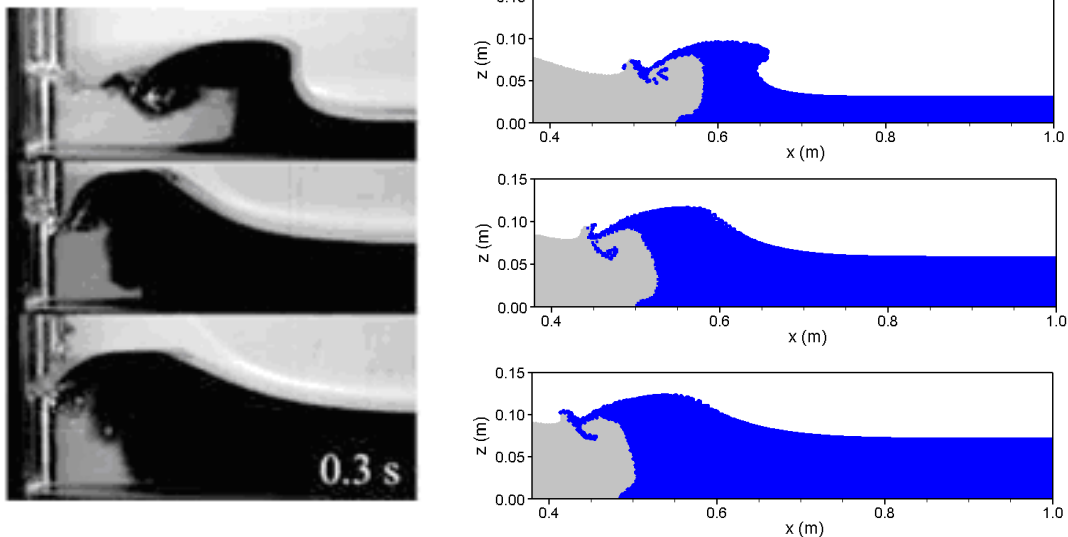
422

423

424

425

426



427 **Figure 6 Experimental (left Jonasi et al., 2004) and numerical (right) mixing patterns at**

428 **$t = 0.3$ s for $h_1 = 0.030$ m (top), 0.058 m (middle) and 0.070 m (bottom)**

429

430 As the wave front travels further downstream, the mixing interface evolves into patterns that

431 are considerably different from the characteristics seen in the early stage. Figure 7 shows the

432 experimental snapshots and the corresponding SPH simulations at $t = 0.60$ s. The mixing

433 interfaces are now located at quite some distance upstream of the propagating wave front.

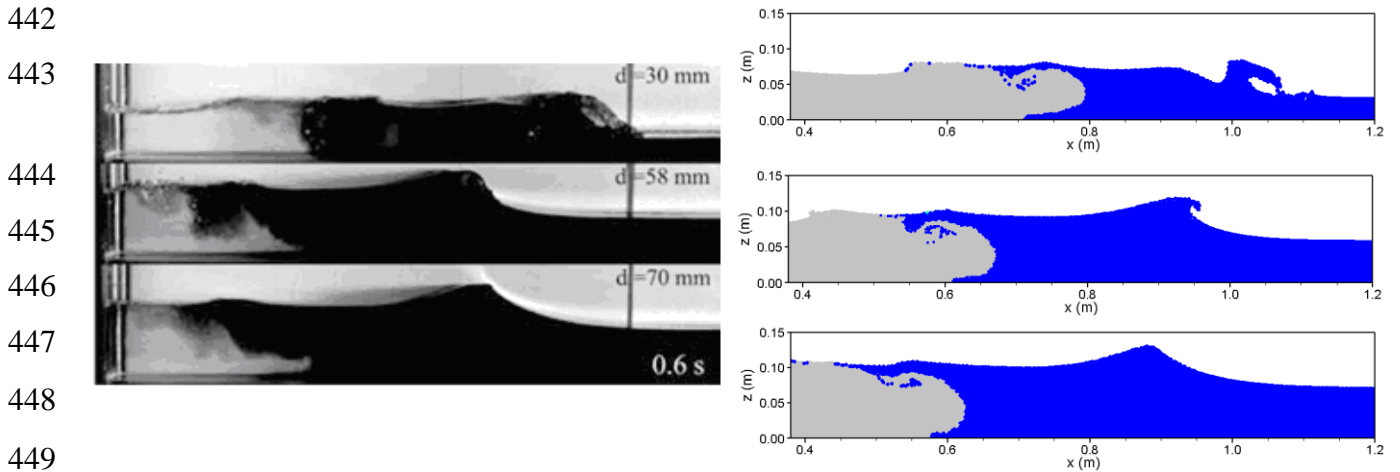
434 The numerical model can still crudely reproduce the mixing dynamics at this time. Figure 7

435 displays mixing interfaces inclining slightly upstream near the free surface. Except for a thin

436 boundary layer immediately above the bed, the upstream water appears to advance faster

437 close to the bottom. Another difference from the early-stage mixing as shown in Figure 6 is

438 that the two water bodies are relatively well mixed by this time. Similar numerical
 439 simulations have also been carried out using the VOF method (Jian and Liang, 2012), which
 440 found that the WCSPH model is computationally more efficient than the VOF model for all
 441 the depths considered.



451 **Figure 7 Experimental (left Jonasi et al., 2004) and numerical (right) mixing patterns at**
 452 **$t = 0.6$ s for $h_1 = 0.030$ m (top), 0.058 m (middle) and 0.070 m (bottom)**

453

454

455 5. Model Application: Dam Break Flow Mixing in a Long Channel

456

457 In this section, the WCSPH model is applied to study the interface development of dam break
 458 flow in a long channel. We will focus on the later stage of the mixing process, when the
 459 interface becomes less chaotic. **Immediately after the dam-break, there is a violent mixing**
 460 **between the reservoir water and tail water due to the formation of the vortices. The later stage**
 461 **is when these violent vortical motions settle down after the flood front has travelled some**
 462 **distance downstream. At this stage, the interface between different water regions is quite**
 463 **clear, and can be approximated by using a straight line.** The study would be useful for
 464 evaluating the hydro-environment in long waterways. The bores in the waterways can be
 465 formed by not only the dam breaks but also tides and tsunamis.

466

467

468 **5.1 Model setup and computational parameters**

469

470 The numerical setup of this hypothetical dam-break problem consists of a 2000 m long
471 horizontal water tank. Water is initially stagnant and separated by a gate located at $x = 1000$
472 m. The initial conditions are thus defined as:

$$473 \quad u(x,0) = 0, \quad h(x,0) = \begin{cases} h_1 & \text{if } x > 1000 \text{ m} \\ h_0 & \text{if } x \leq 1000 \text{ m} \end{cases} \quad (13)$$

474 The initial upstream water depth h_0 is set at 10.0 m throughout the study. Several
475 downstream water depths have been investigated, ranging from 2.0 m ~ 7.0 m. As a reference,
476 the analytical solution to the SWEs (Jian, 2013) is included to evaluate the predictions of dam
477 break wave propagations and the corresponding mixing process.

478

479 In the WCSPH model, a particle size of 0.2 m is used for the best compromise between the
480 computational efficiency and accuracy. The total simulation time is 50.0 s, which ensures that
481 the wave front even under the smallest depth ratio does not reach the downstream end of the
482 channel. The computational time step is $\Delta t = 0.0004$ s.

483

484 **5.2 Discussion on the flow field**

485

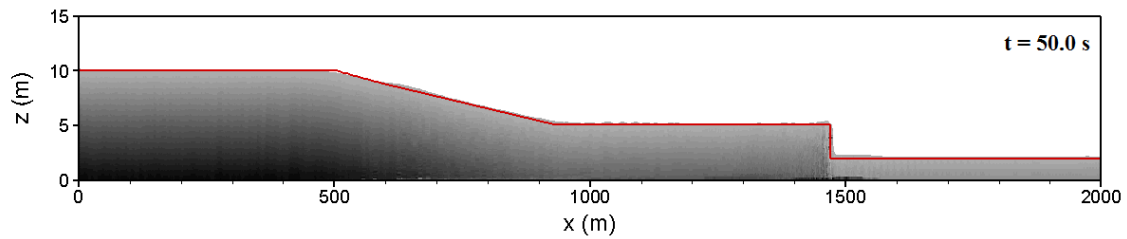
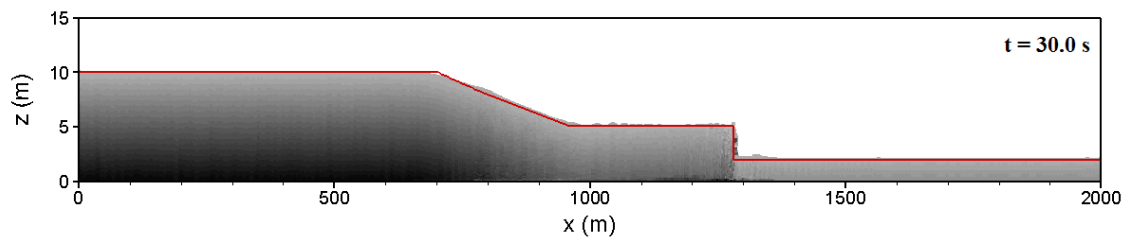
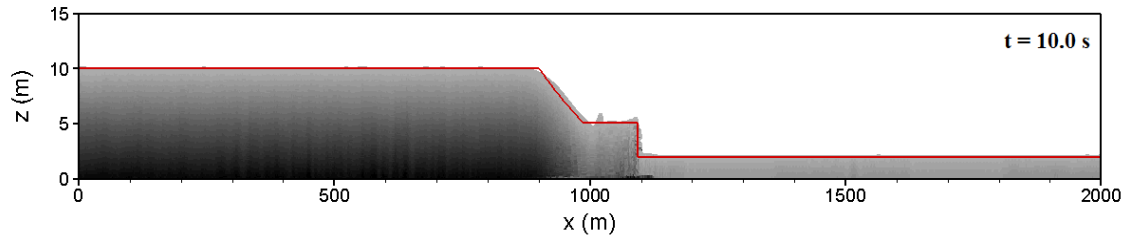
486 The numerical results of the WCSPH model are compared with the analytical solutions to the
487 SWEs. It has been well known that the SWEs model is capable of producing reasonable
488 estimations of the wave propagation at the later stage of dam-break flows when there is less
489 variation in the vertical direction. Three downstream water depths (h_1) are considered for the
490 validation purpose: $h_1 = 2.00$ m, 5.00 m and 7.00 m. The simulations aim to test the shallow
491 water assumptions and provide a full picture of the wave propagations over the shallow,
492 medium and deep water depths.

493

494 For the smallest downstream water depth $h_1 = 2.00$ m, the WCSPH results agree extremely
495 well with the solutions to the SWEs in terms of the surface profiles as shown in Figure 8.
496 However, when the downstream water depths increase to $h_1 = 5.0$ m and 7.0 m, the wave
497 propagations predicted by the WCSPH model in Figures 9 and 10 fall behind the analytical

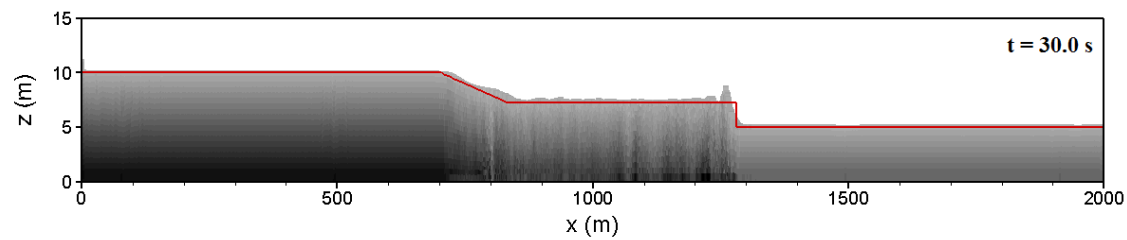
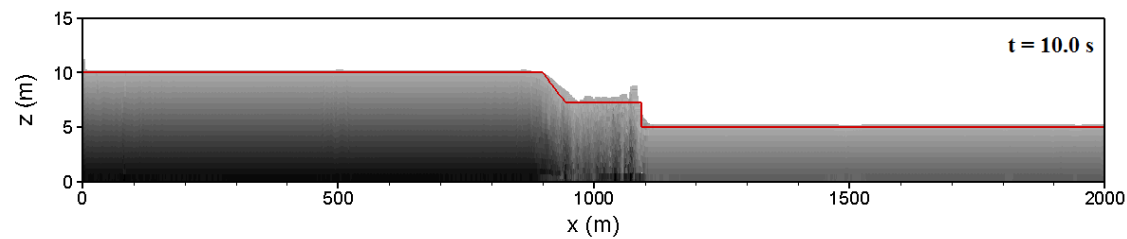
498 predictions according to the SWEs. It is also shown that this difference in the propagation
499 speed increases with time and the downstream water depth.

500

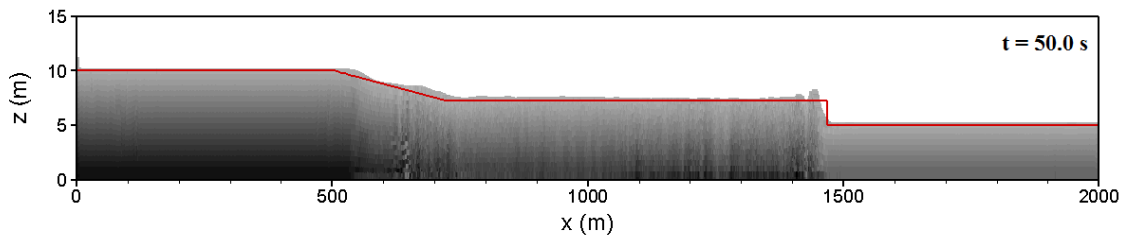


507 **Figure 8 Analytical solutions (solid line) and WCSPH results (shaded area) of surface**
508 **profiles at $t = 10.0$ s, 30.0 s and 50.0 s for $h_0 = 10.0$ m and $h_1 = 2.0$ m**

509



513

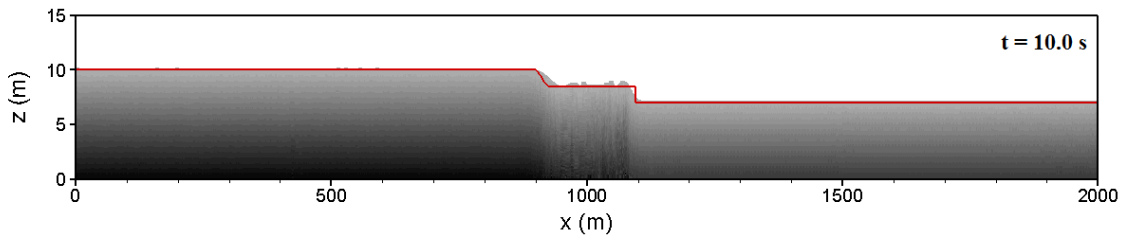


514
515

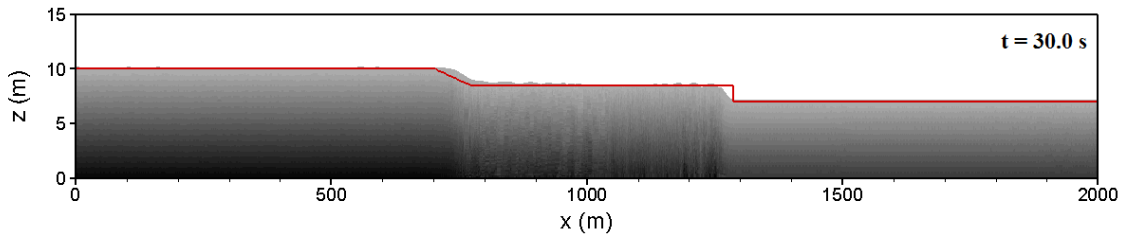
516 **Figure 9 Analytical solutions (solid line) and WCSPH results (shaded area) of surface**
517 **profiles at $t = 10.0$ s, 30.0 s and 50.0 s for $h_0 = 10.0$ m and $h_1 = 5.0$ m**

518

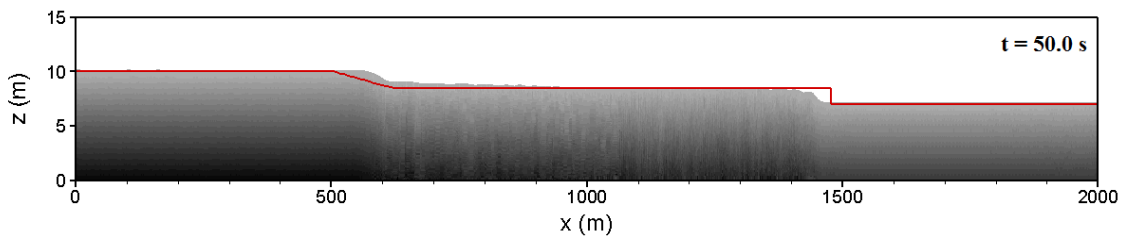
519



520
521



522
523



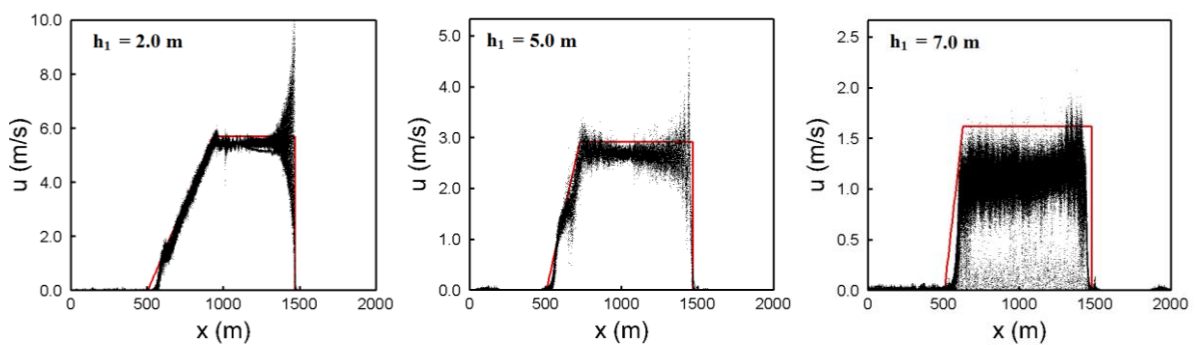
524
525

526 **Figure 10 Analytical solutions (solid line) and WCSPH results (shaded area) of surface**
527 **profiles at $t = 10.0$ s, 30.0 s and 50.0 s for $h_0 = 10.0$ m and $h_1 = 7.0$ m**

528

529 The situations in Figures 8 to 10 are consistent with the horizontal velocity distributions of
530 the three downstream flow depths computed at $t = 50.0$ s, as shown in Figure 11. The
531 average velocity predicted by the WCSPH model agrees well with the SWEs prediction at h_1

532 = 2.0 m, but is 3.3% smaller at $h_1 = 5.0$ m and 25% smaller at $h_1 = 7.0$ m. The discrepancy is
 533 thought to be caused mainly by the over-estimation of fluid bulk speed arisen from the
 534 uniform velocity distribution over the depth in the SWEs. In the previous validation case, the
 535 solutions to the SWEs also tend to give a faster propagation at the deep downstream water
 536 layer when compared with experimental observations. The VOF modelling results in Jian
 537 (2013) also confirms the accuracy of the present WCSPH computations.
 538



539
 540
 541 **Figure 11 Analytical solutions (solid line) and WCSPH results (dot) of the velocity**
 542 **distribution at $t = 50.0$ s for $h_1 = 2.0$ m, 5.0 m and 7.0 m**

543
 544 Here we need to point out that Figures 8 to 10 show some kinds of oscillations around the
 545 wave front in the SPH results while these are not found in the analytic solutions of SWEs.
 546 Due to the assumption of hydrostatic pressure distribution in the SWEs, the SWEs model
 547 always generates a step wave front without numerical dispersion. The refinement of the
 548 SWEs by adding the Boussinesq terms could demonstrate much more satisfactory
 549 performance in the case of rapidly varied flows such as dam break in an open channel, which
 550 was reported in the latest SPH applications in the field (Chang et al., 2014).

551
 552 **5.3 Discussion on the mixing**

553
 554 Disregarding the chemical reaction and molecular diffusion between the upstream and
 555 downstream waters, the mixing interface can be determined solely by the advection of fluid
 556 particles. Here, the evolution of mixing dynamics is analysed with regard to the interface
 557 evolution over the time and the influence of the water depth ratios.

558

559 Figure 12 presents the mixing profiles from $t = 5.0$ s to 50.0 s for the downstream depth $h_1 =$
560 3.0 m and the corresponding horizontal velocity profiles are shown in Figure 13 (sloped lines
561 in the velocity figures indicate the location of interface between the reservoir water and tail
562 water). The early surface profiles indicate that the waveforms have already settled into some
563 well-established propagating fronts, with little wave breaking across the flow field. The
564 velocity profile at $t = 0.0004$ s shows a large gradient in the horizontal velocity field along
565 the initial discontinuity. This reflects the large momentum exerted by the collapsed water on
566 the stagnant downstream flow. The velocity gradient causes the vertically positioned interface
567 to slowly evolve into an inclined slope. By the time $t = 5.0$ s, the surface profile indicates
568 that the interface has already developed into a curve with a larger steepness near the free
569 surface. The velocity profile at $t = 5.0$ s still exhibits a large velocity gradient over the depth.
570 The magnitude within the immediate mixing zone is approximately less than 4.0 m/s at the
571 lower part of the water depth and over 4.5 m/s at the upper part. This drives the mixing
572 interface to incline further downstream. By $t = 10.0$ s, the interface becomes more inclined,
573 mainly driven by the fast-moving fluid particles above the mid-depth. The velocity gradient
574 has reduced by at least 0.3 m/s across the depth in the mixing zone that envelops the interface.
575 From $t = 10.0$ s to 20.0 s, the velocity gradient within the mixing zone has further reduced by
576 approximately 0.2 m/s. Most of the fast-moving particles seen at $t = 10.0$ s have slowed
577 down. Only a small number of them are still visible within 1.0 m beneath the free surface in
578 the velocity profile at $t = 20.0$ s. Beyond $t = 20.0$ s, the mixing interface seems to settle into
579 a relatively stable shape. Little change is observed in the mixing interface from $t = 20.0$ s to
580 50.0 s. The slope of the interface is approximately 32° above the mid-depth while the lower
581 part remains at around 20° . The velocity fields indicate that the flow domain has settled at a
582 horizontal velocity of around 4.4 m/s for the rest of the simulation.

583

584

585

586

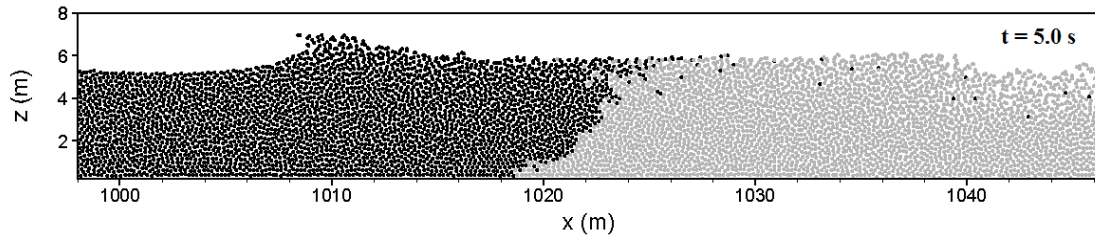
587

588

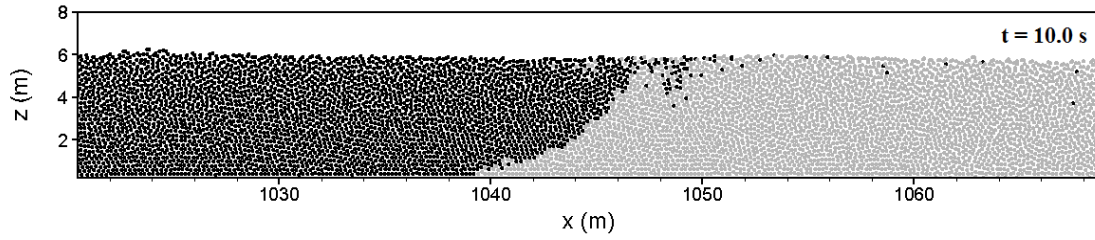
589

590

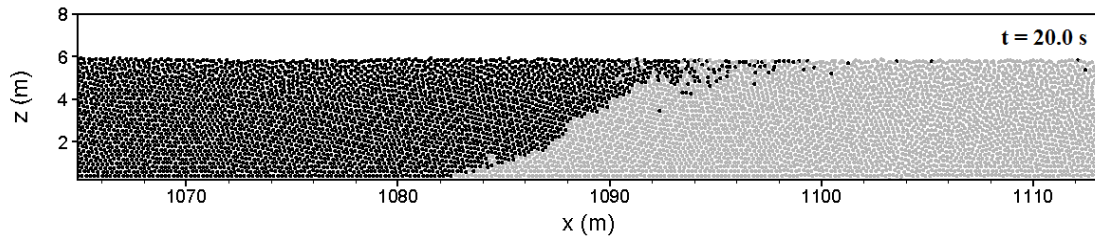
591



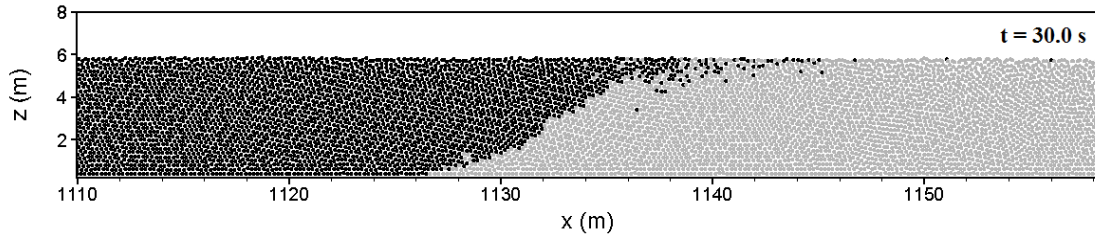
592



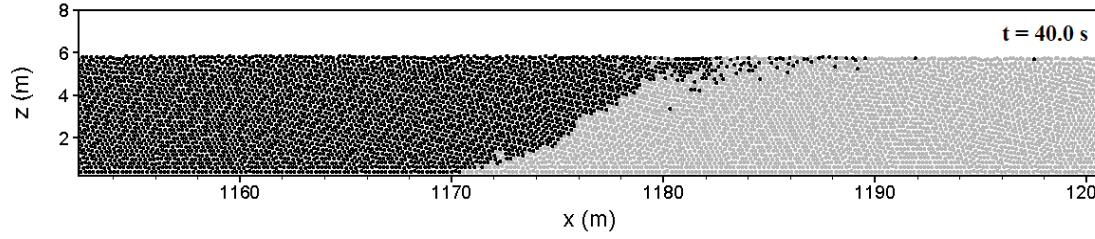
593



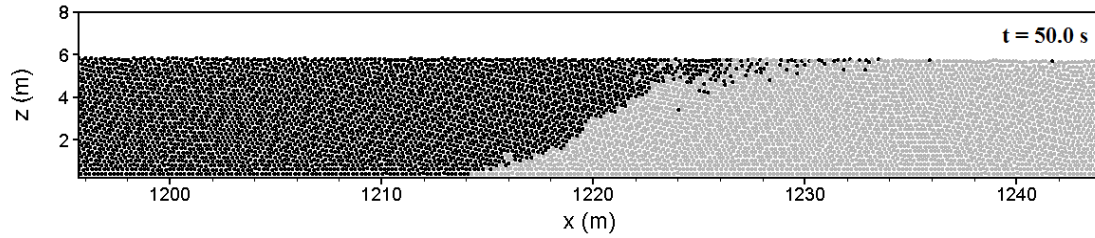
594



595



596



597

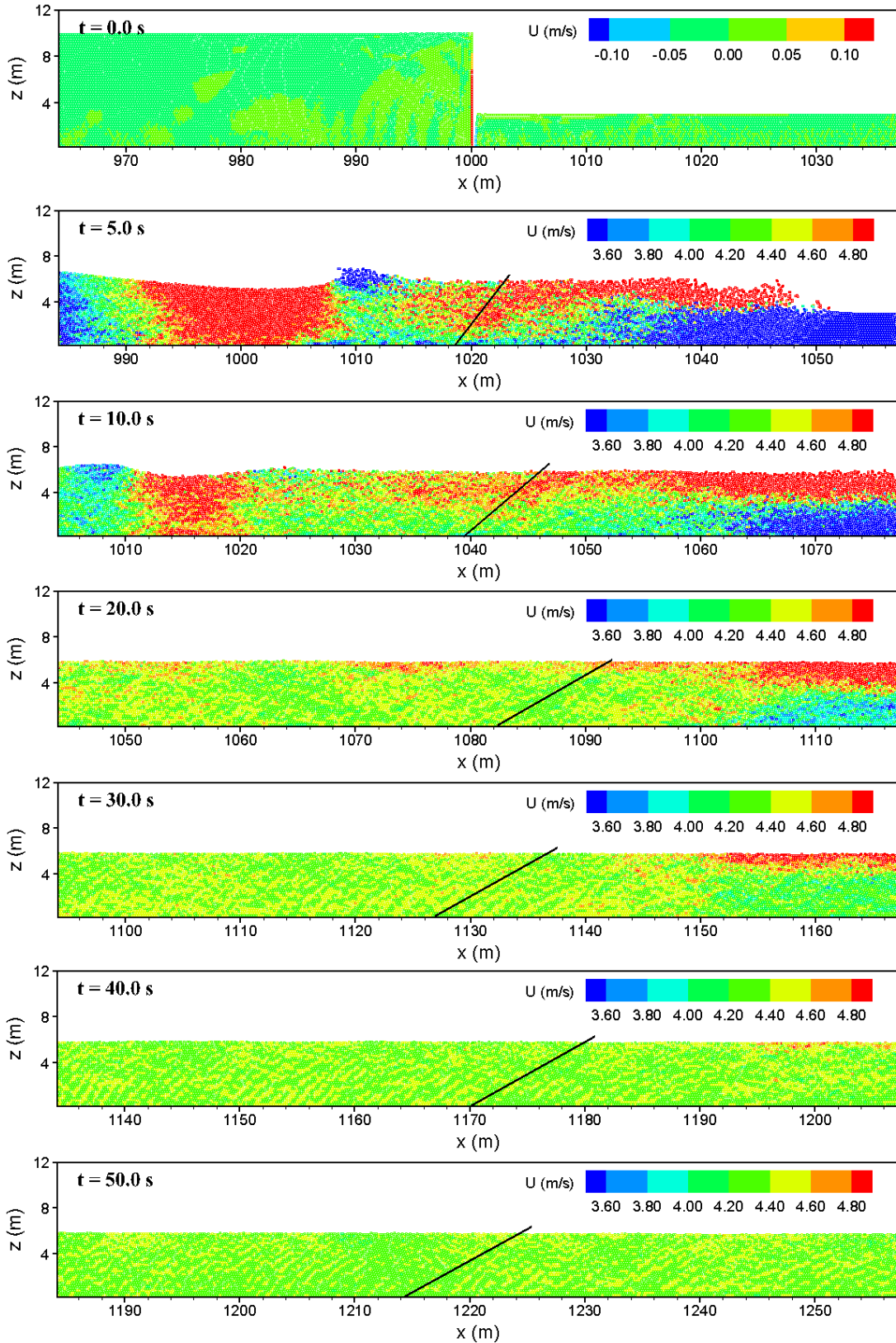
598

599 **Figure 12** Mixing patterns for downstream water depth $h_1 = 3.0$ m at $t = 5.0$ s, 10.0 s,

600

20.0 s, 30.0 s, 40.0 s and 50.0 s

601



602

603

604

605

606

607

608

609

610

611

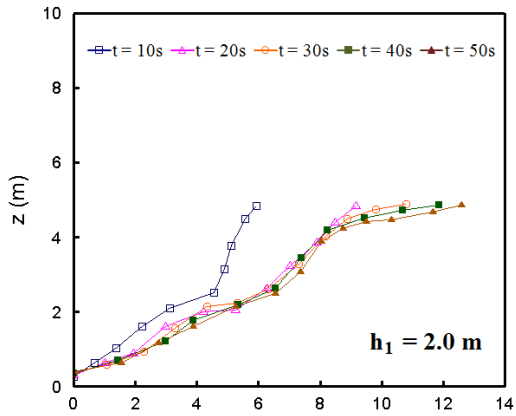
Figure 13 Horizontal velocity distributions for downstream water depth $h_1 = 3.0$ m at $t = 0.0004$ s, 5.0 s, 10.0 s, 20.0 s, 30.0 s, 40.0 s and 50.0 s

612 Similar features of the interface evolution and velocity distribution can also be observed at a
613 larger downstream water depth $h_1 = 6.0$ m. Owing to the larger pressure force and inertia
614 effect of the downstream water body, the interfaces are much steeper than the small depth
615 case at all instants. However, the mixing process still settles into a stable state within the
616 immediate mixing zone by $t = 20.0$ s. The horizontal velocity settles at an equilibrium value
617 of approximately 2.1 m/s beyond $t = 20.0$ s. There is little change to the interfacial curves
618 after this time. The detailed results are not plotted in this paper to save space, but interested
619 readers are referred to Jian (2013).

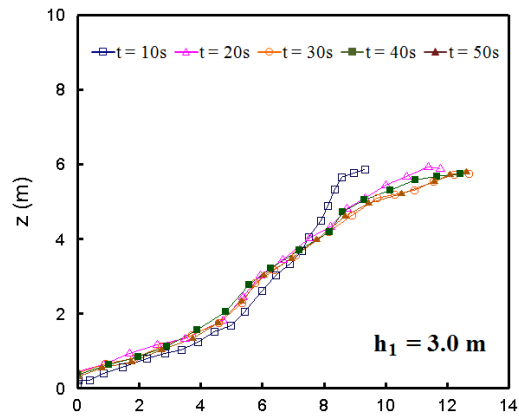
620

621 In summary, the interfaces all take the shape of a forward-leaning line a certain period after
622 the initiation of the dam-break. The mixing interface developments for a range of
623 downstream water depths, varying from $h_1 = 2.0$ m to 7.0 m, are tracked over the time and
624 plotted in Figure 14. The x -axis shows the span of the mixing curve from its most upstream
625 point near the bottom of the channel to its most downstream point at the free surface. In order
626 to minimise the complication at the bottom boundary, the interfaces are tracked from a
627 distance equivalent to one particle size above the solid boundary. Figure 14 shows the
628 evidence that the equilibrium state is reached by $t = 20.0$ s for most of the depth ratios. Very
629 little change in the interface shapes takes place after this time, except for $h_1 = 7.0$ m, where
630 small adjustments can be found at the later time. All interfaces at $t = 10.0$ s demonstrate a
631 change in the slope of the interface above the mid-depth. The lower part of the interfaces
632 undergoes only slight adjustment in the process of reaching their equilibrium forms,
633 especially for $h_1 > 5.0$ m. Most of the changes occur near the free surface, where fluid
634 particles take longer time to slow down. The horizontal span of the mixing interface
635 decreases with the increasing depth ratio (h_1 / h_0), and a larger h_1 / h_0 also corresponds to the
636 faster establishment of the final equilibrium state. These can be explained by the influence of
637 the horizontal velocity gradient in the vertical direction, since a larger downstream water
638 depth gives rise to smaller velocity non-uniformity over the water column. Generally
639 speaking, the mixing dynamics are significantly affected by the horizontal velocity gradient
640 over the water depth. There are no further changes in the interface curve when the
641 equilibrium state is reached in the horizontal velocity field.

642

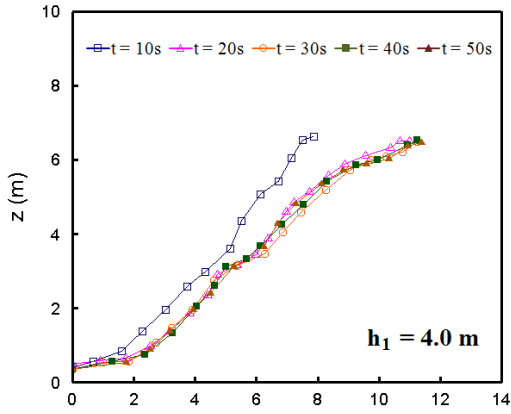


Distance from the most upstream point of the interface (m)

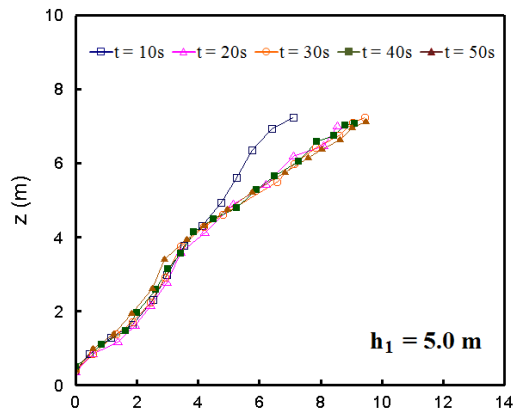


Distance from the most upstream point of the interface (m)

643
644

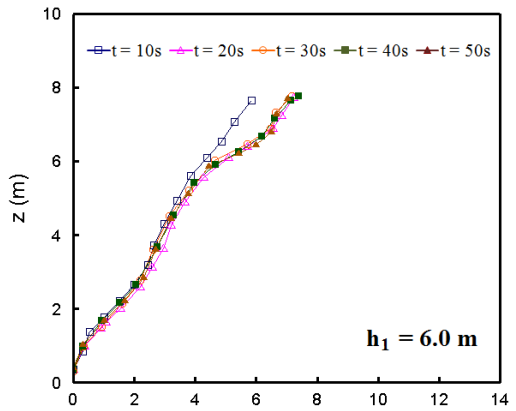


Distance from the most upstream point of the interface (m)

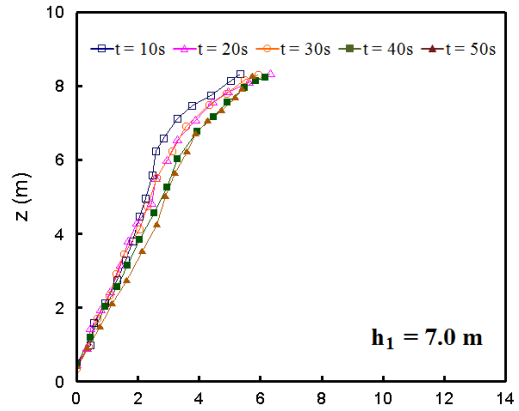


Distance from the most upstream point of the interface (m)

645



Distance from the most upstream point of the interface (m)



Distance from the most upstream point of the interface (m)

646
647

648

Figure 14 Mixing interface developments for $h_1 = 2.0 \text{ m} \sim 7.0 \text{ m}$

649

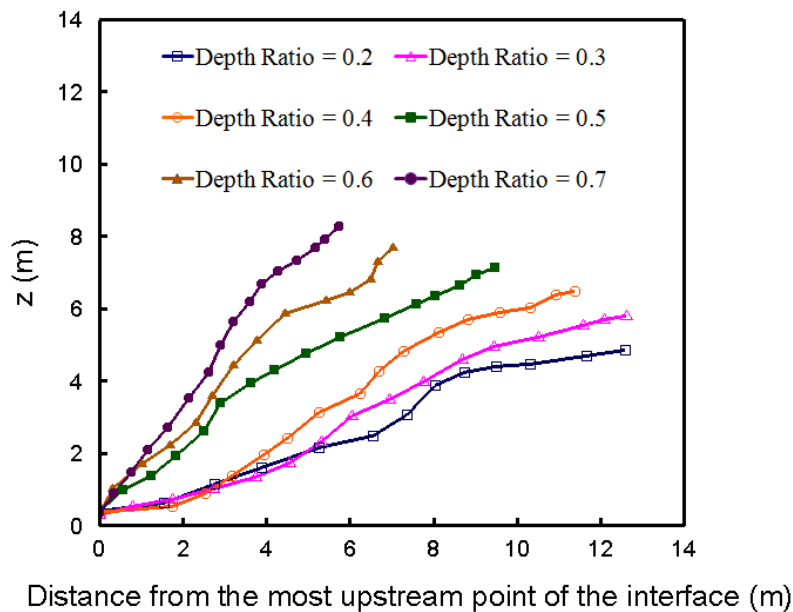
650

651 **5.4 Fully established mixing interface and its dependence on the depth ratio**

652

653 The discussions in the previous section suggest that the initial depth ratio plays an important
654 role in the mixing dynamics in dam-break flows. This section further studies the effect of the
655 initial depth ratios on the final mixing interface at the equilibrium state. Figure 15 shows the
656 mixing profiles at $t = 50.0$ s for different downstream water depth ratios (h_1/h_0). It is
657 evident that the slope of the mixing interface at the equilibrium state is positively correlated
658 to the initial ratio between the downstream and upstream water depths. As discussed earlier,
659 the final forms of the interface are generally determined by the horizontal velocity
660 distributions in the first 20 seconds of the simulation. Figure 16 details the velocity fields of
661 the mixing zone containing the interface for different depth ratios at $t = 10.0$ s.
662 Reading from the scales of the velocity fields as indicated in the legends, it is evident that the
663 magnitude of the velocity gradient decreases with the increasing depth ratio. As a result, the
664 interface reaches the equilibrium state much faster and the slope of the corresponding
665 interface profile is also expected to be steeper for the deep downstream water depth.

666

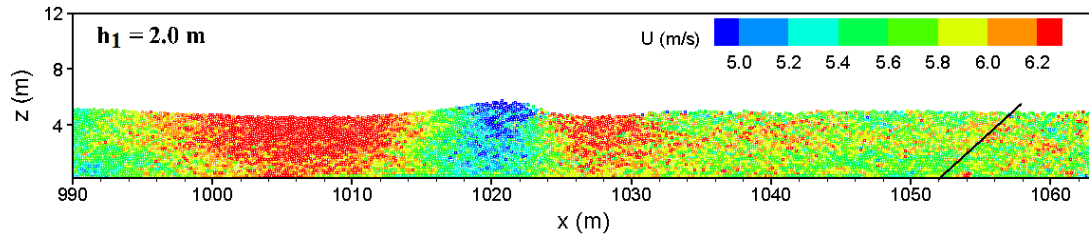


667

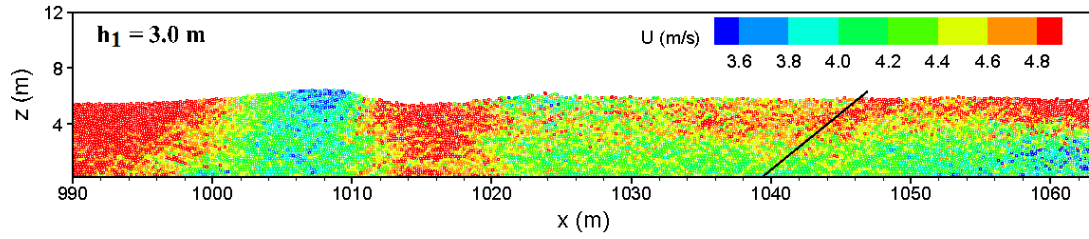
668 **Figure 15 Mixing interface profiles for different depth ratios at $t = 50.0$ s**

669

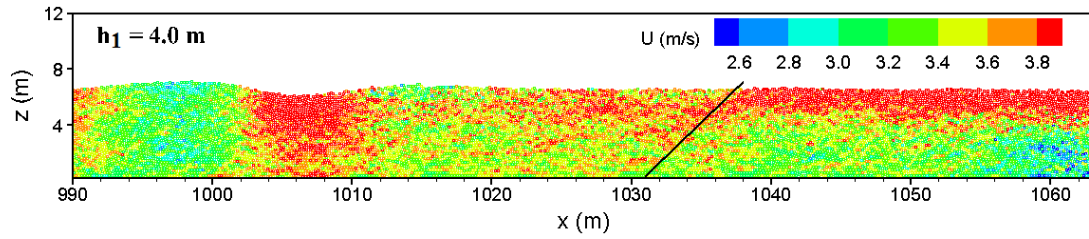
670



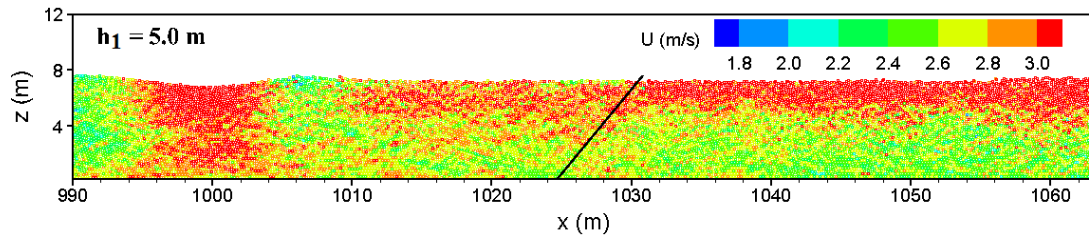
671
672



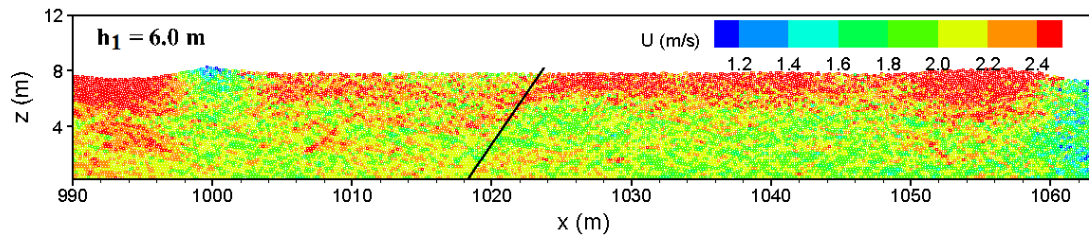
673
674



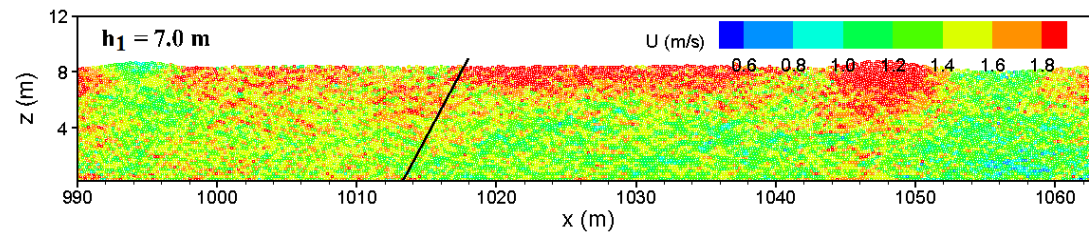
675
676



677
678



679
680

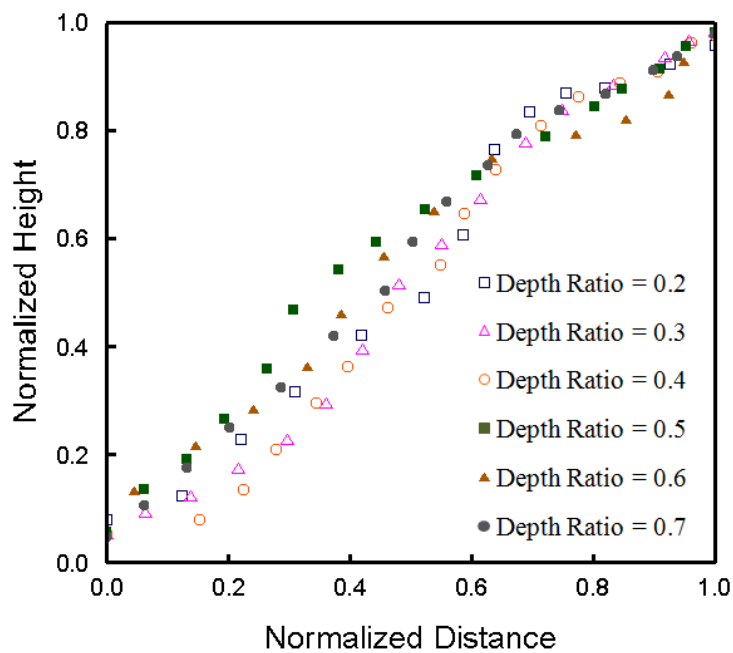


681
682
683
684

Figure 16 Horizontal velocity profiles for different depth ratios at $t = 10.0$ s

685

686 Each of the mixing interface profile in final steady state in Figure 15 can be normalised using
687 the water depth of the mixing zone in the vertical direction and using the span of the interface
688 in the horizontal direction. The normalized curves are plotted in Figure 17, which shows
689 consistently similar forms regardless of the initial depth ratios. The overall angle of the slopes
690 is approximately 45° . There exists a slight change of the slope at 20% of the water depth
691 below the water surface. The slope of the interface becomes milder above this height.



692

693

694 **Figure 17 Normalized mixing interface curves for different depth ratios in equilibrium**

695

696

697

698 **6. Conclusions**

699

700

701 This paper reports on the mixing process involved in both early and later stages of the dam-
702 break flows, using the WCSPH simulations and the analytical solutions to the SWEs. A case
703 study concerning dam-break flow propagation is first carried out to validate the WCSPH
704 model, highlighting its capability of reproducing the surface profiles under different flow

705 conditions. The results from the model agree well with the experimental measurements,
706 analytical solutions to the SWEs and numerical predictions based on the VOF model. Then
707 the mixing process involved in dam-break flows is examined for the period immediately after
708 the gate opening. The performance of the WCSPH model is validated against the
709 experimental results for the near-field dam-break problem, proving its ability of simulating
710 the mixing dynamics with satisfactory accuracy for both the shallow and deep ambient water
711 layers.

712

713 The subsequent application pays attention to the mixing dynamics and the water-water
714 interface development at the later stage of dam-break flow in a long water tank of 2000 m.
715 Six different water depth ratios have been considered in the study. The SWEs tend to predict
716 a faster propagation of the interface, particularly for the larger depth ratios, but they agree
717 well with the WCSPH simulations in the shallow downstream water condition. The numerical
718 results of the WCSPH model show that for all the depth ratios considered, the equilibrium
719 state is reached by approximately $t = 20.0$ s after the instantaneous release. The interface
720 curvature and velocity gradient remain largely unchanged afterwards. The numerical
721 outcomes suggest that the interface develops into a curved slope soon after the simulation
722 starts, driven by the gradient in the horizontal velocity field over the depth. As time elapses,
723 the interface becomes more gradual near the surface as the fluid particles in the mid-depth
724 region slow down more rapidly than the ones at the water surface. The slope of the mixing
725 interface at the equilibrium state becomes steeper with the increasing downstream water
726 depth.

727

728 As for the future research direction, it is recognised that the three-dimensional model is
729 necessary to be able to reproduce a more realistic mixing process in dam break flows in a
730 narrow channel where the side-wall effect is strong and the bed topography is complex.

731

732

733 **Acknowledgements**

734

735 The first author acknowledges the Jafar Studentship during her PhD study at the University of
736 Cambridge. The other authors acknowledge the support of the

737 Major State Basic Research Development Program (973) of China (No. 2013CB036402),
738 Open Fund of the State Key Laboratory of Hydraulics and Mountain River Engineering,
739 Sichuan University (SKHL1404; SKHL1409), Start-up Grant for the Young Teachers of
740 Sichuan University (2014SCU11056) and National Science and Technology Support Plan
741 (2012BAB0513B0).

742

743

744

745 **References**

746

747 Chang, T. J., Chang, K. H. and Kao, H. M. (2014), A new approach to model weakly
748 nonhydrostatic shallow water flows in open channels with smoothed particle hydrodynamics,
749 *Journal of Hydrology*, 519, 1010-1019.

750

751 Chang, T. J., Kao, H. M. and Chang, K. H. (2011), Numerical simulation of shallow-water
752 dam break flows in open channels using smoothed particle hydrodynamics, *Journal of*
753 *Hydrology*, 408, 78-90.

754

755 Colagrossi, A. and Landrini, M. (2003), Numerical simulation of interfacial flows by
756 smoothed particle hydrodynamics, *Journal of Computational Physics*, 191(2), 448-475.

757

758 Crespo, A. J. C. (2008), Application of the Smoothed Particle Hydrodynamics Model
759 SPHysics to Free-surface Hydrodynamics, Ph.D. thesis, Universidade de Vigo.

760

761 Crespo, A. J. C., Gómez-Gesteira, M. and Dalrymple, R. A. (2008), Modelling dam break
762 behaviour over a wet bed by a SPH technique, *Journal of Waterway, Port, Coastal and Ocean*
763 *Engineering*, 134(6), 313-320.

764

765 Dalrymple, R. A. and Rogers, B. D. (2006), Numerical modelling of water waves with the
766 SPH method, *Coastal Engineering*, 53(2-3), 141-147.

767

768 Gingold, R. A. and Monaghan, J. J. (1977), Smoothed particle hydrodynamics: theory and
769 application to non-spherical stars, Royal Astronomical Society Monthly Notices, 181, 375-
770 389.
771

772 Gómez-Gesteira, M. and Dalrymple, R. A. (2004), Using a 3D SPH method for wave impact
773 on a tall structure, Journal of Waterway, Port, Coastal and Ocean Engineering, 130(2), 63-69.
774

775 Jánosi, I. M., Jan, D., Szabó, K. G. and Téli, T. (2004), Turbulent drag reduction in dam-break
776 flows, Experiments in Fluids, 37, 219-229.
777

778 Jian, W. (2013), Smoothed Particle Hydrodynamics Modelling of Dam-break Flows and
779 Wave-structure Interactions, Ph.D. thesis, The University of Cambridge.
780

781 Jian, W. and Liang, D. (2012), On simulating mixing process in dam-break flows,
782 Proceedings of 2nd IAHR Europe Conference, Munich, 27-29 June, 1-6.
783

784 Kao, H. M. and Chang, T. J. (2012), Numerical modeling of dambreak-induced flood and
785 inundation using smoothed particle hydrodynamics, Journal of Hydrology, 448, 232-244.
786

787 Khayyer, A. and Gotoh, H. (2010), On particle-based simulation of a dam break over a wet
788 bed, Journal of Hydraulic Research, 48(2), 238-249.
789

790 Lee, E.-S., Violeau, D., Issa, R. and Ploix, S. (2010), Application of weakly compressible and
791 truly incompressible SPH to 3-D water collapse in waterworks, Journal of Hydraulic
792 Research, 48(Extra Issue), 50-60.
793

794 Liang, D. (2010), Evaluating shallow water assumptions in dam-break flows, Proceedings of
795 the ICE – Water Management, 163(5), 227-237.
796

797 Liang, D., Thusyanthan, I., Madabhushi, S. P. G. and Tang, H. (2010), Modelling solitary
798 waves and its impact on coastal houses with SPH method, China Ocean Engineering,
799 24(2), 353-368.

800

801 Lucy, L. (1977), A numerical approach to the testing of fission hypothesis, *The Astronomical*
802 *Journal*, 82(12), 1013–1024.

803

804 Monaghan, J. J. (1994), Simulating free surface flows with SPH, *Journal of Computational*
805 *Physics*, 110, 399-406.

806

807 Monaghan, J. J. (2000), SPH without a tensile instability, *Journal of Computational Physics*,
808 159(2), 290-311.

809

810 Pu, J., Shao, S., Huang, Y. and Hussain, K. (2013), Evaluations of SWEs and SPH numerical
811 modelling techniques for dam break flows, *Engineering Applications of Computational Fluid*
812 *Mechanics*, 7(4), 544-563.

813

814 Shakibaeinia, A. and Jin, Y. C. (2011), A mesh-free particle model for simulation of mobile-
815 bed dam break, *Advances in Water Resources*, 34(6), 794-807.

816

817 Stansby, P. K., Chegini, A. and Barnes, T. C. (1998), The initial stages of dam-break flow,
818 *Journal of Fluid Mechanics*, 374, 407–424.

819

820 Violeau, D. and Issa, R. (2007), Numerical modelling of complex turbulent free surface flows
821 with the SPH method: an overview, *International Journal for Numerical Methods in Fluids*,
822 53(2), 277–304.